INSTITUTE OF PHYSICS PUBLISHING JOURNAL OF PHYSICS D: APPLIED PHYSICS
J. Phys. D: Appl. Phys. **37** (2004) 1780–1791 PII: S0022-3727(04)72696-0

A Monte Carlo simulation of radiation trapping in electrodeless gas discharge lamps

Kapil Rajaraman[1] **and Mark J Kushner**[2,3]

[1] Department of Physics, University of Illinois, 1110 West Green St., Urbana, IL 61801, USA
[2] Department of Electrical and Computer Engineering, University of Illinois, 1406 West Green St., Urbana, IL 61801, USA

E-mail: rajaramn@uiuc.edu and mjk@uiuc.edu

Received 29 November 2003
Published 16 June 2004
Online at stacks.iop.org/JPhysD/37/1780
doi:10.1088/0022-3727/37/13/009

Abstract
Radiation trapping and transport are important to the power balance of low pressure non-equilibrium plasma lighting sources. This is particularly the case for radio frequency inductively coupled lamps having complex geometries and where control of radiation trapping is an important design consideration. To investigate these issues, a Monte Carlo radiation transport simulation was developed and integrated into a two-dimensional plasma dynamics model. Investigations were performed on the 254 nm ($6\,^3P_1$–$6\,^1S_0$) and 185 nm ($6\,^1P_1$–$6\,^1S_0$) resonance radiation transitions from Hg in Ar/Hg electrodeless discharges. We found that analytically computed radiation trapping factors are less accurate when there is a non-uniform density of absorbers and emitters, as may occur in low pressure lamps, in our case due primarily to cataphoresis. For typical lamp conditions (hundreds of mTorr fill pressure of argon with the vapour pressure of Hg, a few megahertz driving frequency), the electromagnetic skin depth is much larger than the size of the vessel. Therefore, the frequency of excitation does not appreciably affect the distribution of absorbers and emitters, and so has little effect on radiation trapping. Studies were performed on industrially available lamp geometries. We found that the shape of the plasma cavity influences trapping factors, primarily due to the consequences of transport of Hg ions on the distribution of radiators.

1. Introduction

Electrodeless radio frequency (rf) powered gas discharges are finding increasing use as lighting sources, particularly as fluorescent lamps, primarily due to their increased lifetime and improved efficiency. The lack of internal electrodes reduces ageing issues (e.g. electrode sputtering) and reduces power losses from the cathode fall. The devices of interest are fluorescent lamps operating in rare gas–Hg mixtures, usually Ar/Hg [1, 2]. These electrodeless sources typically operate at lower gas pressures (hundreds of mTorr) than those of conventional linear positive column lamps (a few to 10 Torr) and with larger mole fractions of Hg. In such lamps, ultraviolet (UV) resonance radiation from Hg(254 nm, $6\,^3P_1$–$6\,^1S_0$; 185 nm, $6\,^1P_1$–$6\,^1S_0$) is absorbed by phosphors on the internal walls of the lamp. The phosphors in turn generate visible light. The resonance radiation may be absorbed and re-emitted many times in the plasma during its transit from the initial sites of emission to striking the phosphor. This process, commonly called radiation trapping or imprisonment, lengthens the effective lifetime of the excited state as viewed from outside the lamp [3]. The time required for any given quantum of energy to escape the plasma is longer due to this series of absorption and re-emission steps.

Radiation trapping by itself is not necessarily detrimental to the operation of the lamp or to its efficiency. In the absence of other processes, the photons do eventually escape, as in

[3] Author to whom any correspondence should be addressed.

 © 2004 IOP Publishing Ltd Printed in the UK

the steady state the rate of photon escape equals the rate of initial generation of quanta. The longer effective lifetime of the excited states, however, increases the likelihood that collisional processes will quench the excitation prior to escape, thereby reducing the net number of photons escaping the plasma. Second-order effects resulting from the lengthened lifetime of the resonance level include changes in the ionization balance (due to multistep ionization from the excited state) and the electron temperature. (For plasmas with non-Maxwellian electron energy distributions, the electron temperature $T_e = (2/3)\varepsilon$, where ε is the mean electron energy.) Quantifying and perhaps controlling radiation trapping is, therefore, an important design consideration for improving the efficiency of these lamps.

Radiation trapping was first theoretically addressed using a modified form of diffusive transport for the excited states [4]. The method works reasonably well for discharges having low absorber densities where the photon transport has a long mean free path. This method was improved by Holstein and Biberman [5, 6], who accounted for non-local transport of photons and dependence on the lineshape function. Using the Holstein method, the Einstein A-coefficient is decreased (and the lifetime increased) by a geometry dependent factor to account for the absorption and re-emission steps. Analytical expressions for simple geometries are available [7, 8]. The spatial distribution of emitters must be fairly simple to enable the integration of the resulting Green's function for transport of photons. Inherent to this method is the full spectral redistribution of radiation upon re-emission. That is, the frequency of the emitted photon within the lineshape function is independent of the absorption frequency. In cases where there are complex geometries or distributions of radiators and absorbers, one must resort to numerical methods to solve for the decay rates and trapping factors.

Monte Carlo methods, first popularized by Anderson *et al* [9], are well suited to addressing radiation transport where the spatial distributions of absorbers and radiators are complex or change in time, or partial frequency redistribution (PFR) may be important [10–12]. In simple geometries, the distributions for the ground and excited state densities can be estimated or parametrized. In this regard, Lawler and Curry [13] have developed semi-empirical expressions for radiation trapping factors in cylindrical geometries using Monte Carlo and propagator function techniques for fundamental mode distributions and radially symmetric inhomogeneities. They found that the trapped lifetimes of the resonance radiation of Hg in Ar/Hg plasmas, as measured outside the plasmas, are not significantly affected by moderate inhomogeneities in absorber densities, though the excited atom distributions are [12]. They also investigated the transport of photons produced by the 185 nm transition [14] and the consequences of foreign gas broadening [15].

In more dynamic systems, a self-consistent plasma model that accounts for the evolution of gas densities, temperatures and other plasma parameters may be necessary. The need for such coupled models has been recently addressed by Lee and Verboncoeur [16, 17], who developed a radiation transport model coupled to a particle-in-cell simulation, and have applied it to a one-dimensional planar Ar discharge. Their results agree well with Holstein eigenmode analyses for radiation trapping factors.

To address the coupling of radiation transport with plasma kinetics in two dimensions, the Monte Carlo radiation transport module (MCRTM) was developed and interfaced with the Hybrid Plasma Equipment Model (HPEM) [18]. The integrated model is capable of addressing lamps having complex geometries in which the densities of radiators and absorbers are not only non-uniform but highly dependent on the shape of the lamp through processes such as cataphoresis. The combined model was applied to analyses of Hg/Ar lamps having geometries similar to those commercially available (Philips QL and Matsushita Everlight). We found that coupling of the plasma kinetics to the MCRTM led to significant spatial variations in densities and temperatures of photon radiating and absorbing species. In selected cases, these spatial inhomogeneities had measurable effects on radiation trapping. The models used in this investigation are described in section 2 and our results are discussed in section 3. Our concluding remarks are in section 4.

2. Description of the models

The MCRTM tracks a quantum of energy emitted by plasma excited species as the photon is absorbed and re-emitted while traversing the plasma. As the probability for absorption and re-emission depends on local densities of the absorbing and emitting species, the densities of quenching and lineshape perturbing species, and the gas temperature, the MCRTM was interfaced to the HPEM, which provides these quantities. In turn, the MCRTM provides the effective lifetime of emitting excited states for use in the plasma kinetics routines of the HPEM. The HPEM has been described in detail in previous publications, and so will be only briefly discussed here [18].

The HPEM is a two-dimensional modular simulator having three main modules: the electromagnetics module (EMM), the electron energy transport module (EETM), and the fluid kinetics module (FKM). The rf electromagnetic fields and phases are calculated in the EMM module. These fields are then used in the EETM to obtain electron transport coefficients and electron impact source functions. These parameters are then used in the FKM where momentum, continuity, and energy equations are solved for all heavy particles. A drift diffusion formulation for electrons is used to enable an implicit solution of Poisson's equation. The species densities, fluxes and temperatures, and electrostatic fields are then returned to the EMM and EETM modules. Many iterations through the modules are executed until a converged solution is obtained.

The MCRTM directly interfaces with the FKM following its execution during each iteration through the HPEM. The MCRTM receives species densities, gas temperatures, and rate constants from the FKM. With these parameters the frequencies for perturbing and quenching collisions affecting the species participating in radiative transfer reactions are calculated. Using the algorithms described further, the MCRTM produces radiation trapping factors that modify the lifetime of radiating species, which are then used in formulating rate equations during the next execution of the FKM. The algorithms used in the MCRTM are similar to those used by Sommerer [10]. Pseudoparticles representing photons are tracked from their site of emission through multiple absorptions and re-emissions until their escape from the plasma

or until the quantum of energy is quenched. Although reflection from surfaces can be accounted for, we assumed that all surfaces are absorbing or transmitting and so any photon that strikes a surface is lost from the plasma.

Although radiation transport is accounted for in the MCRTM, the photon absorption sources resulting from that transport are not explicitly included in the rate equations for plasma species. Instead, the lifetimes of the radiating species are adjusted consistent with the calculated radiation trapping factors. We have performed test calculations where these photon absorption terms are included in the rate equations for plasma species while keeping their natural lifetimes. Over the range of parameter space of interest to this study, the resulting distributions of radiative species are not significantly different. In a forthcoming publication, this latter technique will be discussed and the specific operating conditions that require the more rigorous approach will be described.

Pseudoparticles are emitted from sites randomly distributed within a numerical mesh cell in proportion to the density of radiators in that cell (obtained from the FKM). As the densities of radiators may vary by orders of magnitude over the plasma region, the number of pseudoparticles released from each cell i is re-scaled to ensure that a statistically relevant number of pseudoparticles is emitted from every cell

$$n_i = n_{\min} + (n_{\max} - n_{\min}) \frac{\log N_i^* - \log N_{\min}^*}{\log N_{\max}^* - \log N_{\min}^*} \qquad (1)$$

where n_i is the number of pseudoparticles emitted from cell i, and $n_{\min}$ and $n_{\max}$ are the pre-selected minimum and maximum number of pseudoparticles permitted to be emitted and N_i^* is the density of the radiating species in cell i. $N_{\min}^*$ and $N_{\max}^*$ are the minimum and maximum densities of N^* in the plasma. These values are dynamically determined during execution of the model. A weighting w_i is assigned to each pseudoparticle for the purposes of collecting statistics. For a pseudoparticle emitted from cell i,

$$w_i = \prod_m w_{m,i} \qquad (2)$$

where w_m is a series of subweightings. The first such subweighting is

$$w_{1,i} = \frac{N_i^* \Delta V_i}{n_i} \qquad (3)$$

where ΔV_i is the volume of cell i.

The frequency of the photon is then selected from the lineshape function $g(\nu)$, which is the probability of a photon being emitted at a frequency ν [19]. The likelihood of the photon being emitted near the line centre can be hundreds to thousands of times higher than that for being emitted in the far wings of the lineshape. The majority of photons escaping the plasma usually originate from the wings of the lineshape, where absorption probabilities are smaller. Selecting pseudoparticles with probabilities directly proportional to $g(\nu)$ would, in the absence of using a very large number of pseudoparticles, undersample the wings of the lineshape. For example, at the line centre, the mean free path for the absorption of 254 nm resonance radiation is as short as 100 μm. Photons having mean free paths sufficiently long to escape the lamp (many mm to 1 cm) have $g(\nu)/g(\nu_0) < 0.001$. Statistically, this means that the number of photons emitted in the wings of the profile would require many tens-of-thousands of pseudoparticles per numerical cell; there are many thousand such cells in a typical two-dimensional mesh.

Although the assignment of frequency directly proportional to $g(\nu)$ is the least ambiguous method, the need to avoid sampling problems in two dimensions and the desire to obtain frequency resolution throughout the mesh motivates one to try another method. To avoid statistical under-sampling in the wings of the lineshape profile using a reasonable number of particles, we instead uniformly distribute the pseudoparticles over a pre-selected range of frequencies about the line centre ν_0, and use an additional weighting factor $w_2 = g(\nu)$ to account for the likelihood of emission at a given frequency. This method is essentially equivalent to directly sampling the lineshape while reducing computer time. The centre of the lineshape may be statistically under-sampled but since these photons are absorbed and re-emitted many times, this statistical error is minimal.

The lineshape is a Voigt profile, which combines the features of Doppler and Lorentzian broadening and is applicable at the temperatures and pressures of interest to us. This lineshape is given by

$$g(\nu') = \frac{\gamma}{\pi^{3/2}} \int_{-\infty}^{\infty} \frac{\mathrm{e}^{-y^2}}{\gamma^2 + (\nu' - y)^2}\, \mathrm{d}y,$$
$$\gamma = \frac{\nu_{\mathrm{H}}}{4\pi \Delta\nu_{\mathrm{D}}}, \quad \nu' = \frac{\nu - \nu_0}{\Delta\nu_{\mathrm{D}}} \qquad (4)$$

where ν_{H} is the homogeneous Lorentzian damping frequency, $\Delta\nu_{\mathrm{D}}$ is the Doppler width, and ν' is the frequency departure from ν_0 in units of Doppler width. For our conditions,

$$\nu_{\mathrm{H}} = A + \sum_j 2\nu_j \qquad (5)$$

where A is the Einstein coefficient for spontaneous emission and ν_j is the frequency for broadening collisions by the jth species. As ν_j depends on the local densities and temperatures of collision partners and ν' depends on the local gas temperature through $\Delta\nu_{\mathrm{D}}$, $g(\nu')$ is then also a function of position. Rather than recompute $g(\nu')$ at every mesh point, $g(\nu')$ was pre-computed at the beginning of each iteration of the MCRTM and stored as a two-dimensional array with γ and ν' as interpolation parameters. We estimate the range of ν' to construct the look-up tables based on estimates of densities and temperatures from previous cases. Typical ranges are $-5 \leqslant \nu' \leqslant 5$. Given the array $g(\gamma, \nu')$, the actual value of the Voigt profile at any spatial point is found by simple interpolation using the local values of γ and ν'. For investigations of systems with multiple isotopes or radiating species, $g(\gamma, \nu')$ is pre-computed as a three-dimensional array with the third index corresponding to a given species.

Given the randomly chosen initial frequency, the polar and azimuthal angles for emission are randomly chosen assuming an isotropic distribution. A running tally of the residence time of the pseudoparticle in the plasma is initialized as $\tau_{\mathrm{T}} = -(w_i/A)\ln(r)$, where r is a random number distributed on (0,1). The photon transport is then tracked until its next absorption by stepping through the mesh. As the geometry of the lamp is, in principle, arbitrary, the stepping method is required to account for striking physical objects

(e.g. protruding electrodes). Although view factors and a Green's function could, in principle, substitute for the spatial integration, the trade-offs between computer storage requirements and computing time to derive the Green's function were not favourable.

The null collision method was employed for photon transport. The photon path at frequency ν is advanced a distance $\lambda = \lambda_{\min}(\nu)\ln(r)$, where $\lambda_{\min}(\nu)$ is the minimum mean free path for absorption at frequency ν based on densities, temperatures and cross-sections throughout the mesh

$$\lambda_{\min}(\nu) = \frac{1}{\max(\sum_j N_j \sigma_j(\nu))}, \qquad \sigma_j(\nu) = \frac{A_j c^2 g(\nu)}{8\pi\nu^2} \quad (6)$$

where the max function samples all locations in the mesh and the sum is over absorbing species having density N_j, absorption cross-section $\sigma_j(\nu)$, and Einstein coefficient A_j. After advancing the trajectory a distance λ to location $\vec{r}$, the probability of a real absorption is determined by comparing

$$r < \frac{\sum_j N_j(\vec{r})\sigma_j(\vec{r},\nu)}{\max(\sum_j N_j\sigma_j(\nu))} \quad (7)$$

where r is a random number distributed (0,1). If the inequality is satisfied, the absorption occurs. If not, another test absorption length is chosen and the photon is advanced without change in direction. The identity of the absorbing species k is determined from

$$\delta_{k-1} < r < \delta_k, \qquad \delta_k = \frac{\sum_{j=1}^{k} N_j(\vec{r})\sigma_j(\vec{r},\nu)}{\sum_{j=1}^{n} N_j(\vec{r})\sigma_j(\vec{r},\nu)} \quad (8)$$

where n is the total number of absorbing species. If the absorbing species is non-emitting, the pseudoparticle is removed from the simulation. Otherwise, the photon is re-emitted if not quenched.

At sufficiently large pressures or plasma densities, or statistically long lifetimes, quanta of energy may be quenched by collisions prior to re-emission. The likelihood of this occurring is determined by

$$r > \frac{A'}{A' + \sum_j \nu_j}(\vec{r}), \qquad A' = A\ln(r) \quad (9)$$

where ν_j is the frequency of the jth quenching collision. If the inequality holds, the excited state was deemed to have been quenched prior to emission, and the quantum of energy is removed from the simulation. For non-quenched quanta, τ_T is incremented as $\tau_T \rightarrow \tau_T - (w_{ij}/A)\ln(r)$, and the photon is re-emitted at a frequency determined by PFR.

The trapping factor as viewed from outside the lamp is defined as

$$K = \frac{\sum_m \tau_{T_m}}{\sum_m w_m} A, \quad (10)$$

where the sum is over all escaping photons. For purposes of extension of the lifetime of the excited state, the sum is over all emitted photons. The effective radiative lifetime of the radiating state is then A/K for the next iteration for the HPEM.

The Holstein–Biberman model [5] assumes complete frequency redistribution, that is the frequency and velocity of the emitted photon is uncorrelated to that of the absorbed photon. As such, the frequency for pressure broadening collisions should be commensurate with or larger than the rate of radiative relaxation. PFR assumes that there is a correlation between the absorbed and emitted wavelengths. In the limit of there being no momentum changing collisions, the absorption and emission frequencies should be the same, or at best differ by the natural linewidth. We addressed PFR using two methods. In the first method, photons absorbed at frequency ν, are randomly re-emitted in the frequency range $\nu \pm \Delta\nu$. The value of $\Delta\nu$ was found by determining the trapping factor of the 254 nm transition of Hg in a cylinder of radius R_0 with a uniform density of Hg and Ar, and comparing with a more exhaustive formalism for PFR [20]. The calibration in this manner yielded $\Delta\nu = \alpha\Delta\nu_D$, $1.75 < \alpha < 2.0$. A comparison of the trapping factors so derived and those obtained by Lister [20] for standard fluorescent lamps are shown in table 1. The computed results are also benchmarked against those obtained using the Holstein's method for similar geometries assuming a predominantly Doppler broadened mechanism [20]. The results of Lister use the semi-analytic theory of Menningen and Lawler [14] and Lawler *et al* [15]. In general, the agreement is good.

We also used a more exact formalism for PFR, which is similar to the Jefferies–White approximation [3, 21]. The core of the lineshape is determined by Doppler broadening, while the wings are determined by Lorentzian broadening. The analytic form of the redistribution function is difficult to integrate into a Holstein formulation and so approximations are required. The redistribution function is, therefore, split into a completely coherent and a completely redistributed part. Pure Doppler broadening corresponds to a complete coherence in the rest frame of the atom, but due to the direction of re-emission being random, the absorbed and re-emitted frequencies are uncorrelated in the laboratory rest frame. Thus, pure Doppler broadening corresponds to CFR. We modelled the Doppler core using CFR, and the wings using PFR. To model PFR in the wings for absorption at ν, we redistribute the emission frequency randomly within

Table 1. Comparison of trapping factors obtained by MCRTM, Lister, and the Holstein formulation (in the Doppler broadened regime) for the 254 nm line[a].

R_0 (cm)	[Hg][b] (cm^{-3})	[Ar] (cm^{-3})	T_{ave} (K)	k_{Lister}	k_{MCRTM}	$k_{Holstein}$
0.80	0.28×10^{14}	1.6×10^{17}	373	14.2	14.3	19.0
1.27	0.28×10^{14}	1.3×10^{17}	373	22.3	23.1	32.2
1.91	0.38×10^{14}	8.0×10^{16}	313	47.8	48.8	80.4
2.50	0.38×10^{14}	9.6×10^{15}	313	100.4	104.3	109.1

[a] Lister, private communication using the method described in [14, 15].

[b] Hg density per isotope. Total Hg density is 5 times larger.

one Doppler width of ν. By using the analytic form of the redistribution function, the approximate core cut-off frequency is pre-calculated based on the solution of the equation [21]

$$\exp(-x_\nu^2) = \frac{\gamma}{x_\nu^2\sqrt{\pi}} \tag{11}$$

where x_ν is the departure from the line centre in units of $\Delta\nu_D$.

A lamp may have many radiating species, each having its own spectral distributions for absorption and emission, such as the 254 and 185 nm resonance transitions. In the event these distributions overlap, they may interfere or contribute to radiation transport from another species. This is particularly the case for isotopes whose line centre frequencies are closely spaced. In our model we treated isotopes as separate species to account for, e.g. energy exchanging collisions. For example, when a photon is deemed to have been absorbed, we checked to determine which of the isotopes of the particle is absorbed by using equation (8).

Hyperfine splitting (hfs) of an isotope results in subclasses of the species having a different ν_0, collision frequency and concentration, which leads to different lineshapes for each hfs component. In the same manner as isotopes, we consider each hyperfine component as a separate radiating species. Foreign gas collisions are known to redistribute the excitation on hfs components of odd isotopes [14]. As such, if the quantum was absorbed by an even isotope, it was re-emitted by the same isotope. If the quantum was absorbed by an odd isotope, the likelihood of a collision redistributing the excitation among hfs components was computed using cross-sections from Sommerer [10]. Based on the choice of a random number, if the collision is deemed to have occurred, the excitation is redistributed.

The reaction mechanism for Ar/Hg plasmas is summarized in table 2. The electron impact cross-sections for Hg were taken from Rockwood [22], Kenty [23] and Vriens and Smeets [24]. The heavy-body cross-sections (excitation transfer, quenching) were taken from Sommerer [10]. The values for the cross-section for resonance broadening between Hg species is 3×10^{-14} cm^2 and that for Ar–Hg broadening is 7×10^{-15} cm^2.

Table 2. Reaction mechanism for Ar/Hg plasmas.

Reaction	Rate coefficient[a]	Ref.
e + Ar → Ar + e	b	[25]
e + Ar → Ar(4s) + e	b	[26]
e + Ar → Ar$^+$ + e + e	b	[27]
e + Ar(4s) → Ar + e	b	[26][c]
e + Ar(4s) → Ar$^+$ + e + e	b	[28][d]
e + Hg(6 ^{1}S$_0$) → Hg(6 ^{1}S$_0$) + e	b	[22]
e + Hg(6 ^{1}S$_0$) → Hg(6 ^{3}P$_0$) + e	b	[22]
e + Hg(6 ^{1}S$_0$) → Hg(6 ^{3}P$_1$) + e	b	[22]
e + Hg(6 ^{1}S$_0$) → Hg(6 ^{3}P$_2$) + e	b	[22]
e + Hg(6 ^{1}S$_0$) → Hg(6 ^{1}P$_1$) + e	b	[22]
e + Hg(6 ^{1}S$_0$) → Hg(6 ^{3}D$_J$, 7 ^{3}S$_1$) + e	b	[22]
e + Hg(6 ^{1}S$_0$) → Hg$^+$ + e + e	b	[22]
e + Hg(6 ^{3}P$_0$) → Hg(6 ^{3}P$_0$) + e	b	[22]
e + Hg(6 ^{3}P$_0$) → Hg(6 ^{1}S$_0$) + e	b	[23][c]
e + Hg(6 ^{3}P$_0$) → Hg(6 ^{3}P$_1$) + e	b	[23][c]
e + Hg(6 ^{3}P$_0$) → Hg(6 ^{3}P$_2$) + e	b	[22]
e + Hg(6 ^{3}P$_0$) → Hg(6 ^{1}P$_1$) + e	b	[23]
e + Hg(6 ^{3}P$_0$) → Hg(6 ^{3}D$_J$) + e	b	[23]
e + Hg(6 ^{3}P$_0$) → Hg(7 ^{3}S$_1$) + e	b	[23]
e + Hg(6 ^{3}P$_0$) → Hg$^+$ + e + e	b	[24]
e + Hg(6 ^{3}P$_1$) → Hg(6 ^{3}P$_1$) + e	b	[22]
e + Hg(6 ^{3}P$_1$) → Hg(6 ^{1}S$_0$) + e	b	[23][c]
e + Hg(6 ^{3}P$_1$) → Hg(6 ^{3}P$_0$) + e	b	[23][c]
e + Hg(6 ^{3}P$_1$) → Hg(6 ^{3}P$_2$) + e	b	[22]
e + Hg(6 ^{3}P$_1$) → Hg(6 ^{1}P$_1$) + e	b	[23]
e + Hg(6 ^{3}P$_1$) → Hg(6 ^{3}D$_J$) + e	b	[23]
e + Hg(6 ^{3}P$_1$) → Hg(7 ^{3}S$_1$) + e	b	[23]
e + Hg(6 ^{3}P$_1$) → Hg$^+$ + e + e	b	[24]
e + Hg(6 ^{3}P$_2$) → Hg(6 ^{3}P$_2$) + e	b	[22]
e + Hg(6 ^{3}P$_2$) → Hg(6 ^{1}S$_0$) + e	b	[23][c]
e + Hg(6 ^{3}P$_2$) → Hg(6 ^{3}P$_0$) + e	b	[23][c]
e + Hg(6 ^{3}P$_2$) → Hg(6 ^{3}P$_1$) + e	b	[23][c]
e + Hg(6 ^{3}P$_2$) → Hg(6 ^{1}P$_1$) + e	b	[23][c]
e + Hg(6 ^{3}P$_2$) → Hg(6 ^{3}D$_J$) + e	b	[23]
e + Hg(6 ^{3}P$_2$) → Hg(7 ^{3}S$_1$) + e	b	[23]
e + Hg(6 ^{3}P$_2$) → Hg$^+$ + e + e	b	[23]
e + Hg(6 ^{1}P$_1$) → Hg(6 ^{1}P$_1$) + e	b	[22]
e + Hg(6 ^{1}P$_1$) → Hg(6 ^{1}S$_0$) + e	b	[22][c]
e + Hg(6 ^{1}P$_1$) → Hg(6 ^{3}P$_0$) + e	b	[22][c]
e + Hg(6 ^{1}P$_1$) → Hg(6 ^{3}P$_1$) + e	b	[22][c]
e + Hg(6 ^{1}P$_1$) → Hg(6 ^{3}P$_2$) + e	b	[22][c]
e + Hg(6 ^{1}P$_1$) → Hg$^+$ + e + e	b	[24]
e + Hg(6 ^{3}D$_J$) → Hg(6 ^{3}D$_J$) + e	b	[22]
e + Hg(6 ^{3}D$_J$) → Hg(6 ^{1}S$_0$) + e	b	[22][c]
e + Hg(6 ^{3}D$_J$) → Hg(6 ^{3}P$_0$) + e	b	[22][c]
e + Hg(6 ^{3}D$_J$) → Hg(6 ^{3}P$_1$) + e	b	[22][c]
e + Hg(6 ^{3}D$_J$) → Hg(6 ^{3}P$_2$) + e	b	[22][c]
e + Hg(6 ^{3}D$_J$) → Hg$^+$ + e + e	b	[24]
e + Hg(7 ^{3}S$_1$) → Hg(7 ^{3}S$_1$) + e	b	[22]
e + Hg(7 ^{3}S$_1$) → Hg(6 ^{1}S$_0$)+ e	b	[22][c]
e + Hg(7 ^{3}S$_1$) → Hg(6 ^{3}P$_0$) + e	b	[22][c]
e + Hg(7 ^{3}S$_1$) → Hg(6 ^{3}P$_1$) + e	b	[22][c]
e + Hg(7 ^{3}S$_1$) → Hg(6 ^{3}P$_2$) + e	b	[22][c]
e + Hg(7 ^{3}S$_1$) → Hg$^+$ + e + e	b	[24]
Ar(4s) + Ar(4s) → Ar$^+$ + Ar + e	5.0×10^{-10}	[e]
Ar(4s) + Hg(6 ^{1}S$_0$) → Hg$^+$ + Ar + e	9.0×10^{-10}	[29]
Ar(4s) + Hg → Hg$^+$ + Ar + e	9.0×10^{-10}	[29][f]
Hg* + Hg* → Hg$^+$ + Hg(6 ^{1}S$_0$) + e	3.5×10^{-10}	[30][i]
Ar$^+$ + Hg(6 ^{1}S$_0$) → Hg$^+$ + Ar	1.5×10^{-11}	[31]
Ar$^+$ + Ar → Ar + Ar$^+$	4.6×10^{-10}	[32]
Hg$^+$ + Hg → Hg + Hg$^+$	1.0×10^{-9}	[f,g]
Hg(6 ^{3}P$_1$) → Hg(6 ^{1}S$_0$) + $h\nu$	8.0×10^6 s^{-1}	10[h]
Hg(6 ^{1}P$_1$) → Hg(6 ^{1}S$_0$) + $h\nu$	7.5×10^8 s^{-1}	10[h]
Hg(7 ^{3}S$_1$) → Hg(6 ^{3}P$_0$) + $h\nu$	2.0×10^7 s^{-1}	[33]
Hg(7 ^{3}S$_1$) → Hg(6 ^{3}P$_1$) + $h\nu$	6.0×10^7 s^{-1}	[33]
Hg(7 ^{3}S$_1$) → Hg(6 ^{3}P$_2$) + $h\nu$	5.0×10^7 s^{-1}	[33]
Hg(6 ^{3}D$_J$) → Hg(6 ^{3}P$_0$) + $h\nu$	2.2×10^7 s^{-1}	[33]
Hg(6 ^{3}D$_J$) → Hg(6 ^{3}P$_1$) + $h\nu$	6.6×10^7 s^{-1}	[33]
Hg(6 ^{3}D$_J$) → Hg(6 ^{3}P$_2$) + $h\nu$	2.0×10^7 s^{-1}	[33]

[a] Rate coefficients have units of (cm^3 s^{-1}) unless noted otherwise.
[b] Rate coefficients are calculated in the EETM using cross-sections from the indicated references.
[c] Cross-section obtained by detailed balance.
[d] By analogy with potassium.
[e] Estimated as a gas phase kinetic rate constant.
[f] Hg here represents all states.
[g] Estimated.
[h] Untrapped value which is modified by the MCRTM.
[i] Hg* refers to each of the states 6 ^{3}P$_0$, 6 ^{3}P$_1$, 6 ^{3}P$_2$, 6 ^{1}P$_1$, 6 ^{3}D$_J$, and 7 ^{3}S$_1$.

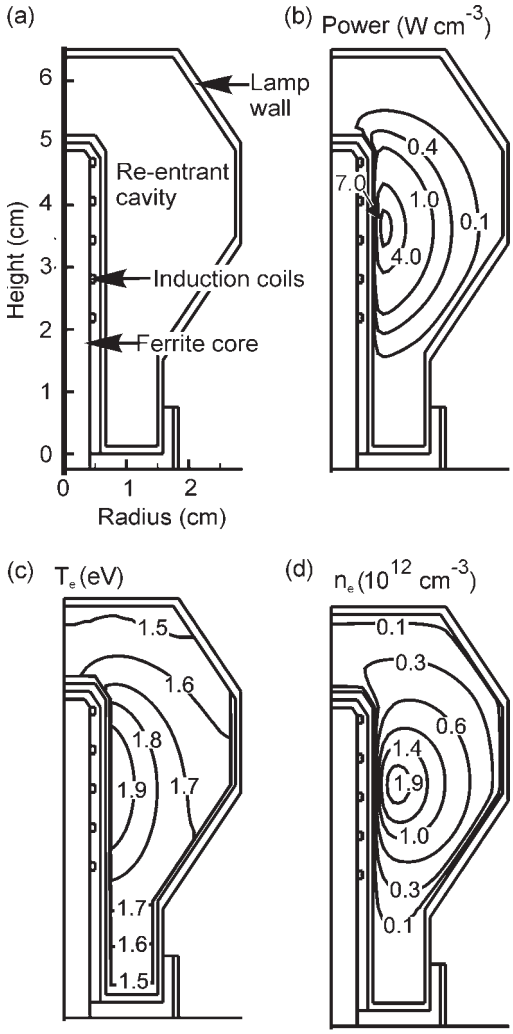

Figure 1. Lamp geometry and plasma properties for the base case conditions (Ar 500 mTorr, Hg 5 mTorr, 55 W). (*a*) Schematic of the lamp, (*b*) power deposition, (*c*) electron temperature and (*d*) electron density. Even though the skin depth exceeds the dimensions of the lamp, power deposition peaks at inner radii due to geometrical considerations. Contour labels are in units shown at the top of each figure.

Table 3. Base case operating conditions.

Ar fill pressure	500 mTorr
Hg vapour pressure	5 mTorr
Cold spot temperature	310 K
RF frequency	5 MHz
Power deposition	55 W

3. Radiation transport in electrodeless lamps

The geometry for the base case is shown in figure 1. This lamp is similar in shape to the Philips QL lamp [34]. The rf coils are wrapped around a central ferrite core. The plasma volume has a re-entrant cavity surrounding the coil. The base case operating conditions are listed in table 3. The skin depth for these conditions is ≈30 cm. The electric field is a maximum near the coils, primarily for geometrical reasons as opposed to a short absorption length. As a result, the largest specific power deposition is near the re-entrant coil, as shown in figure 1.

The electron temperature T_e and density n_e are also shown in figure 1. T_e has a maximum value of ≈2 eV near the coil. For these conditions, the electron mean free path is $\approx 10^{-2}$ cm, much less than the skin depth, and the electron collision frequency is $\approx 1 \times 10^9\ s^{-1}$, much larger than the rf frequency. Power deposition is, therefore, dominantly collisional. The electron density peaks at $\approx 2 \times 10^{12}\ cm^{-3}$ in an annulus around the antenna. The gas mixture is not attaching and recombination in the bulk plasma is negligible. As a result, the dominant charged particle loss is by diffusion. The lower ionization threshold of Hg and multistep ionization from Hg(6P) produces far more rapid ionization than Ar. Any excited states or ions of Ar are rapidly quenched by Penning ionization ($\tau \approx 25\ \mu$s) and charge exchange ($\tau \approx 400\ \mu$s).

Ground and excited state densities of Hg are shown in figure 2. The Hg ground state density [Hg($6\,^1S_0$)] is significantly depleted in the central region of the plasma due to cataphoresis. The ambipolar radial ion flux (see figure 2(*d*)) to the walls at the mid-height of the antenna is $\approx 10^{17}\ cm^2\ s^{-1}$ and the momentum transfer cross-section to Hg($6\,^1S_0$) is $\approx 10^{-15}\ cm^2$, producing a rate of momentum transfer of $\approx 10^2\ s^{-1}$, which is rapid compared to the rate of thermal diffusion. The Hg($6\,^1S_0$) is, therefore, depleted in the central part of the lamp, an effect that is exacerbated by a gas temperature rise with respect to the walls of ≈40 K. Ions recombining on the surfaces provide a source of ground state neutrals at the wall. The end result is that the Hg($6\,^1S_0$) density is maximum near the walls.

The production of Hg($6\,^3P_1$), the upper state of the 254 nm transition, is dominated by electron impact from the ground state. The quenching of Hg($6\,^3P_1$) is dominated by super-elastic electron collisions ($\tau \approx 1$ ms), and radiative relaxation, both of which have rates that are large compared to transport. The density of Hg($6\,^3P_1$), therefore, peaks where the excitation rates are largest, which in this case is near the walls at the height of the antenna where the electron mean energy and Hg($6\,^1S_0$) are largest. The Hg($6\,^1P_1$) density (upper state of the 185 nm transition) also peaks near the antenna. The untrapped (1.3 ns) radiative lifetime of the Hg($6\,^1P_1$) state is small compared to the untrapped lifetime of the Hg($6\,^3P_1$) (125 ns). As a result, spreading by diffusion of the Hg($6\,^1P_1$) density from its peak has a smaller extent than does the Hg($6\,^3P_1$) density, but otherwise the spatial distributions of the two emitting states have the same functional dependences. As a result, we shall only be showing the Hg($6\,^3P_1$) profile as an indication of emitter densities.

Radiation trapping factors were investigated for the 185 and 254 nm transitions while varying the cold spot temperature T_c, which controls the vapour pressure of Hg. As the lamps are sealed, an increase in T_c increases the Hg density while the Ar density remains the same. As such, with increasing T_c the rate of collisional broadening remains nearly constant with a small increase due to the increase in thermal speed. When keeping the power constant, the density of emitters (excited states) is approximately constant. The end result is that the trapping factors increase with T_c, as shown in figure 3. The trapping factors for both the 185 and 254 nm transitions change by nearly the same percentage, and this is to be expected because the spatial profiles of the radiators and absorbers for both the transitions are nearly the same. At

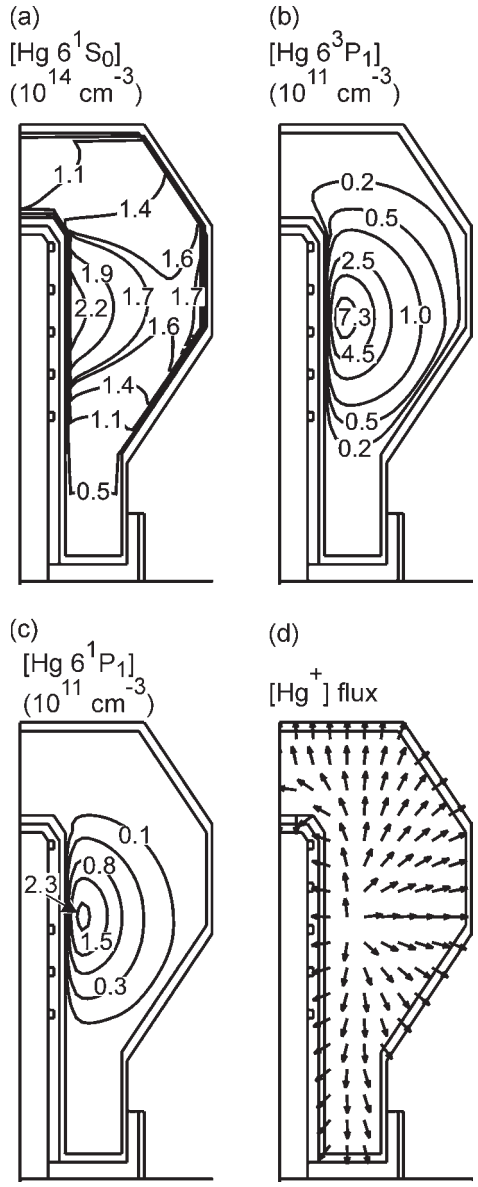

Figure 2. Plasma properties for the base case conditions. (*a*) [Hg($6\,^1S_0$)], (*b*) [Hg($6\,^3P_1$)], (*c*) [Hg($6\,^1P_1$)] and (*d*) flux vectors for Hg^+. The flux vectors show direction only and not magnitude. Cataphoresis and temperature rise decrease the density of ground state Hg. Contour labels are in units shown at the top of each figure.

the largest Hg densities, the total trapped lifetimes ($K\tau$) of the 185 and 254 nm transitions are approximately the same (2.9 μs). Note that at high Hg densities and when resonance broadening dominates, the trapping factor for the 185 nm transition will saturate [14]. The precise value of cold spot temperature at which this saturation occurs depends on the rate of foreign gas broadening and geometry. When extending our calculations to higher temperatures, we obtain saturation in the trapping factor for the 185 nm transition at $T_c \approx 360$ K ($[Hg] = 4 \times 10^{15}$ cm^{-3}).

The trapping factor for the 185 nm line is about 100 times larger than the trapping factor for the 254 nm line, which suggests an inverse scaling of the trapping factor with vacuum radiative lifetime. The Holstein theory for a cylindrical discharge states that the trapping factor for a

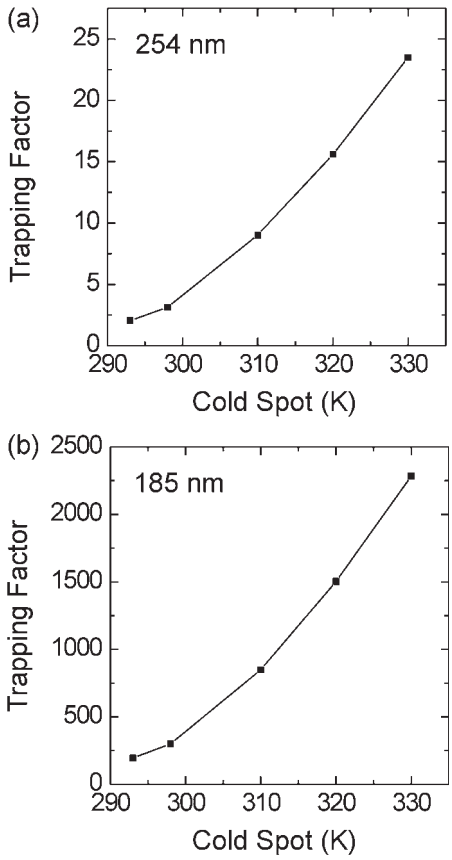

Figure 3. Trapping factors as a function of cold spot temperature for the (*a*) 254 nm and (*b*) 185 nm transition. Increasing absorber density increases radiation trapping factors.

Doppler broadened line scales as

$$K = \frac{\alpha(\pi \ln \alpha)^{1/2}}{1.6}, \qquad \alpha = \frac{R\lambda_0^3 N g_2 A}{8\pi^{3/2} g_1 V_t} \tag{12}$$

where $V_t = (2kT/M)^{1/2}$, λ_0 is the wavelength at the line centre, g_1 and g_2 are the statistical degeneracies for the upper and lower energy levels, and R is the radius of the cylindrical discharge. So, for similar absorber densities, trapping factors should scale almost inversely with the vacuum radiative lifetime, which we observe here. The non-linearities in the scaling of K/[Hg] probably result from the complex non-cylindrical geometry of the lamp and the fact that the densities of absorbers and emitters are not uniform. Using the Holstein formulation for a Doppler-broadened lineshape in a cylindrical geometry with radius 2.5 cm (Hg = 5 mTorr, Ar = 500 mTorr, T = 310 K), the trapping factor for the 254 nm transition should be ≈15. The lower trapping factor obtained from the MCRTM is a consequence of the non-cylindrical geometry and the highly non-uniform distribution of radiators and absorbers. Due to the re-entrant antenna, radiation transport in the middle of the lamp is probably better addressed analytically as a slab of thickness ≈2 cm. When using the Holstein formulation for these conditions, the trapping factor is ≈10. Considering that the radiators have a maximum density displaced <1 cm from the wall where the absorber density has a minimum, the trapping factor implied using the slab analogy could be as small as 4.

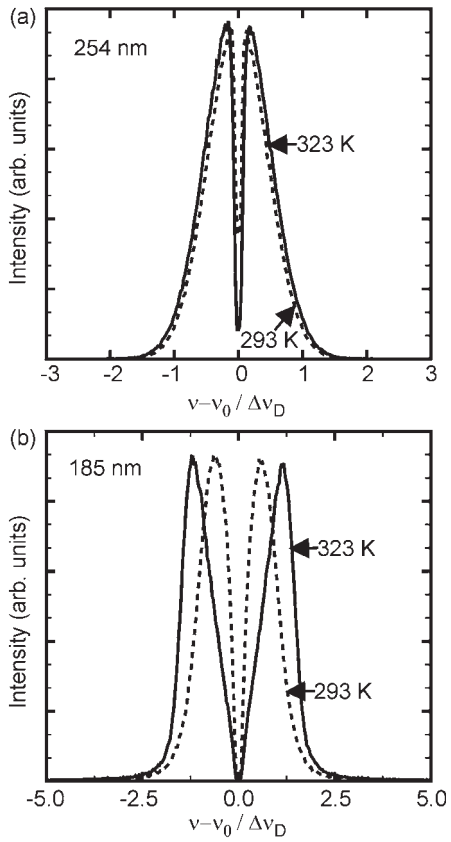

Figure 4. Spectra averaged over photons escaping from the lamp for cold spot temperatures of 293 and 323 K for the (*a*) 254 nm and (*b*) 185 nm transitions. The 185 nm line reversal is more sensitive to the increase in absorber density.

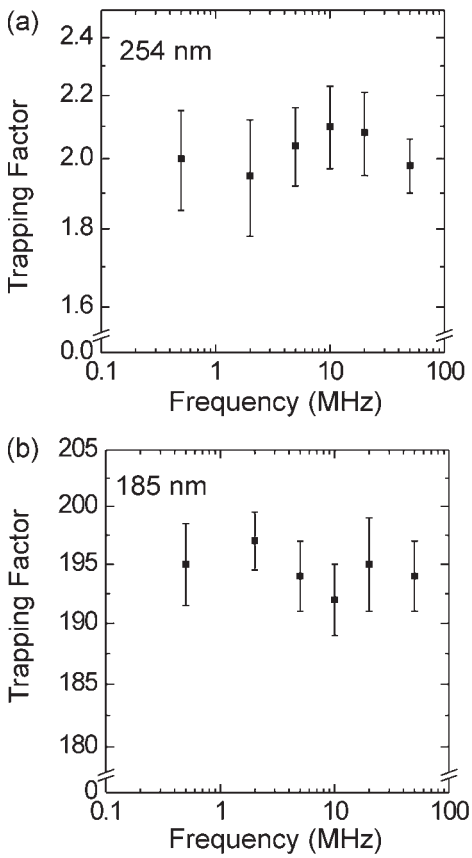

Figure 5. Trapping factors as a function of rf source frequency for the (*a*) 254 nm and (*b*) 185 nm transitions for the base case conditions. No systematic variations in trapping factor with rf frequency were observed.

The spectra for the 254 and 185 nm transitions, averaged over all photons escaping the lamp, are shown for cold spot temperatures of 293 and 323 K (Hg densities of $\approx 3.5 \times 10^{13}$ cm^{-3} and $\approx 3.5 \times 10^{14}$ cm^{-3}, respectively) in figure 4. The dip in the centre of the lineshape is due to the more frequent absorption of photons which, with PFR, may be re-emitted in the wings of the lineshape where the mean free path for absorption is longer and so the likelihood for escape from plasma is greater.

The choice of rf frequency for exciting the plasma is an important design consideration with respect to the efficiency of power transfer. Radiation transport ultimately depends on the spatial distribution of radiators and absorbers, which is determined by the spatial distribution of power deposition. To investigate whether the rf frequency should be a consideration with respect to radiation transport, the frequency was varied while keeping the other parameters constant. The resulting trapping factors for the 254 and 185 nm lines are shown in figure 5. The trapping factors have only small variations with the rf frequency, mostly within the limits of statistical error of the method. At our operating conditions of hundreds of mTorr, the plasma is collisional, and the electron–neutral momentum transfer frequency ν_m is greater than the plasma frequency ω_{pe} near the boundary. In this case, the skin depth is given by

$$\delta_c = \left(\frac{2}{\omega \mu_0 \sigma_{dc}}\right)^{1/2}, \qquad \sigma_{dc} = \frac{e^2 n_e}{m \nu_m} \tag{13}$$

For our lamp, the maximum electron density for the base case operating conditions is 2×10^{12} cm^{-3}. The minimum collision frequency is 1.5×10^7 s^{-1}, which gives a minimum possible skin depth of approximately 30 cm, which is much larger than the size of the lamp. Frequencies in the GHz regime would be required to perturb the spatial distribution of radiators. As a result, radiation transport is little affected by the rf frequency.

Although there are many constraints and trade-offs in lamp design, radiation transport is one important consideration. In this regard, we compared a geometry similar to the Everlight lamp geometry [1] with that of the QL lamp. The Everlight lamp has its coils in an external solenoidal configuration. For purposes of this study, we chose the radius and height of the lamps to be the same. Without a re-entrant void for the central post, the volume of the Everlight lamp is larger. Plasma parameters (power, electron density, [Hg($6\,^1S_0$)] and [Hg($6\,^3P_1$)]) for the Everlight lamp are shown in figure 6 for the base case conditions. Power deposition peaks at ≈ 2.6 W cm^{-3}, which is smaller compared to the QL lamp because the same power (55 W) is deposited into a larger overall volume. Since the peak electric fields are at the outer radii for the Everlight lamp and inner radii for the QL lamp, the incremental volumes for peak power deposition are also larger. The electron density has a similar peak value as the QL lamp though the maximum is displaced to a larger radius. As such, the ion flux producing cataphoresis, which transports Hg($6\,^1S_0$) has inward and outward components. The spatial distribution of

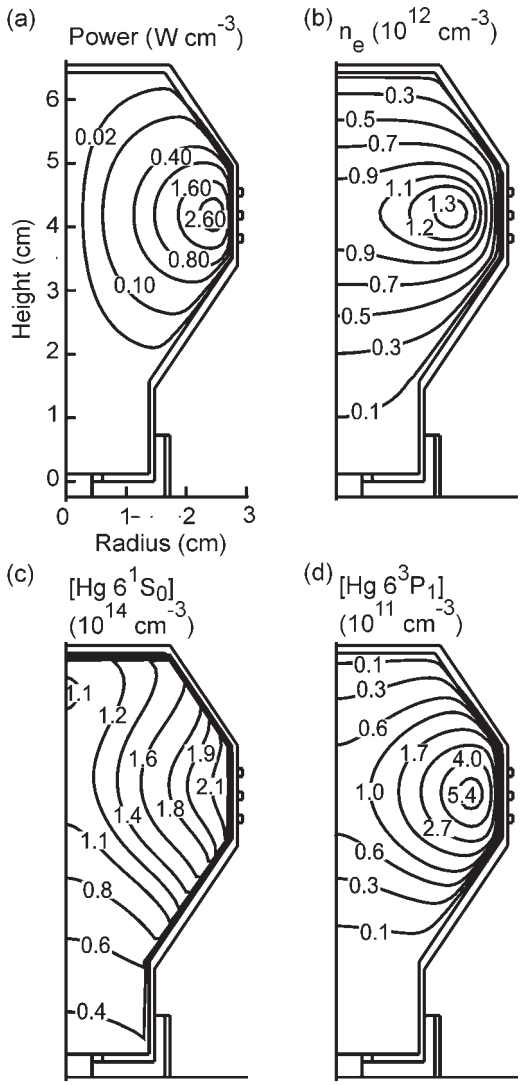

Figure 6. Plasma parameters for the Everlight geometry for the base case conditions (Ar 500 mTorr, Hg 5 mTorr, 55 W). (*a*) Power deposition, (*b*) electron density, (*c*) [Hg($6\,^1S_0$)] and (*d*) [Hg($6\,^3P_1$)]. The change in coil location changes the distribution of radiators and absorbers. Contour labels are in units shown at the top of each figure.

Table 4. Trapping factors for QL and Everlight geometries (55 W, 5 MHz).

Lamp geometry	Hg vapour pressure (mTorr)	Ar fill pressure (mTorr)	Trapping factor K	
			254 nm	185 nm
Everlight	5	100	2.52	220
Everlight	5	500	2.10	203
Everlight	20	100	10.87	1038
Everlight	20	500	10.02	946
QL	5	100	2.46	212
QL	5	500	2.03	194
QL	20	100	9.84	886
QL	20	500	9.03	848

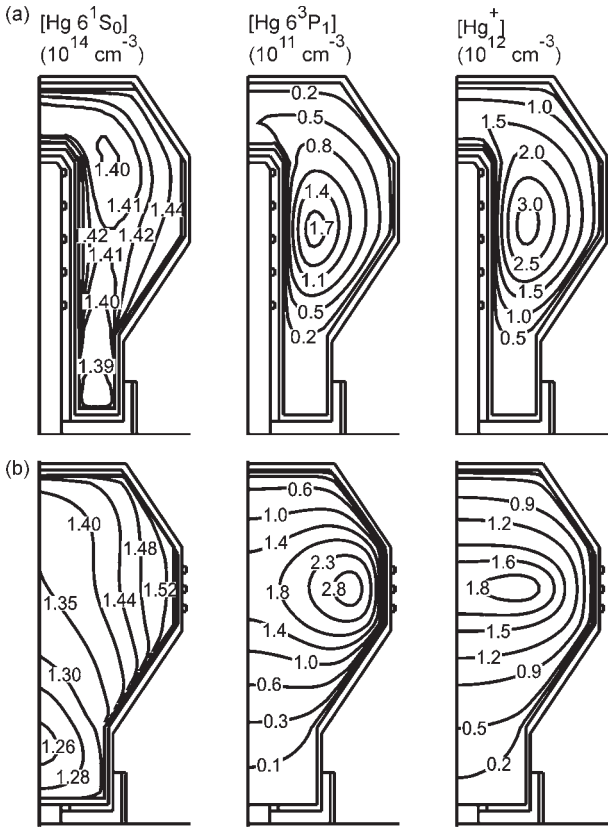

Figure 7. Densities of Hg($6\,^1S_0$), Hg($6\,^3P_1$) and Hg^+ for the (*a*) QL and (*b*) Everlight geometries for 100 mTorr Ar fill pressure, and 5 mTorr Hg(310 K cold spot). Contour labels are in units shown at the top of each figure.

Hg($6\,^3P_1$), though still highly peaked towards the coils, is more uniformly distributed through the volume of the lamp.

Trapping factors for the 254 and 185 nm transitions for the QL and Everlight geometries, obtained while varying the Ar fill pressure and the cold spot temperature are shown in table 3. All other parameters were kept at their base case values. The general trends are that trapping factors decrease with increasing Ar fill pressure and increase with increasing Hg partial pressure. The decrease in trapping with fill pressure results from the increasing Ar collision frequency, which redistributes quanta to the wings of the lineshape, thereby increasing the likelihood for escape. An increase in trapping factor with increasing [Hg] is due to the larger absorber density. The increase in trapping factor did not directly scale with the increase in Hg vapour density. The trapping factors for the QL geometry are systematically smaller than for the Everlight geometry by 5–15%. We attribute these scalings to the non-uniform distributions of radiators and absorbers (table 4).

For example, the Hg ground and excited state densities for the two lamps with an Ar fill pressure of 100 mTorr, and Hg partial pressure of 5 mTorr ($T_c = 310$ K) are shown in figure 7, and for a Hg pressure of 20 mTorr ($T_c = 330$ K) in figure 8. The spatial distributions of the Hg ground state are significantly different between the 5 and 20 mTorr cases. These differences are due in part to the more collisional conditions for electrons with the higher Hg pressure, producing shorter mean free paths for energy dissipation. As a result, excitation is confined closer to the high electric field regions near the coils. The difference in ground state density is also in part due to momentum transfer from ions. Owing to the increase in

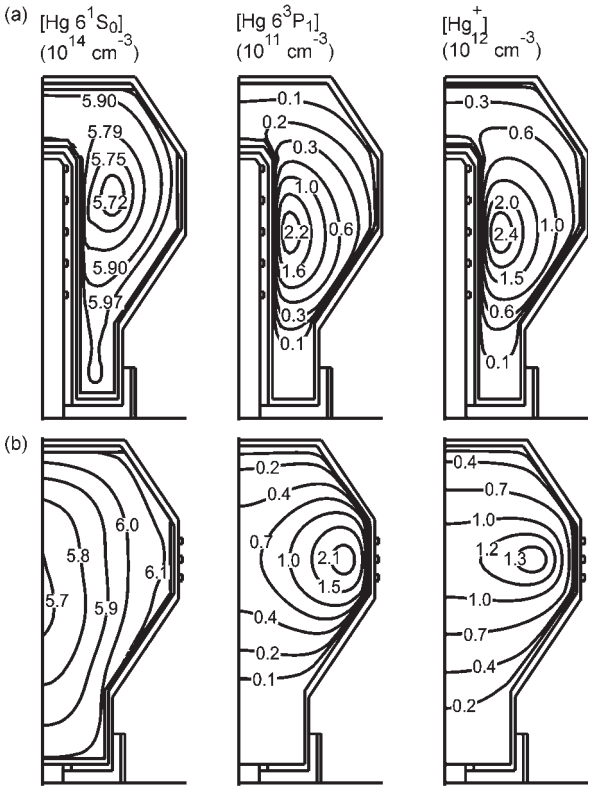

Figure 8. Densities of Hg($6\,^1S_0$), Hg($6\,^3P_1$) and Hg^+ for the (*a*) QL and (*b*) Everlight geometries for 100 mTorr Ar fill pressure, and 20 mTorr Hg(330 K cold spot). Contour labels are in units shown at the top of each figure.

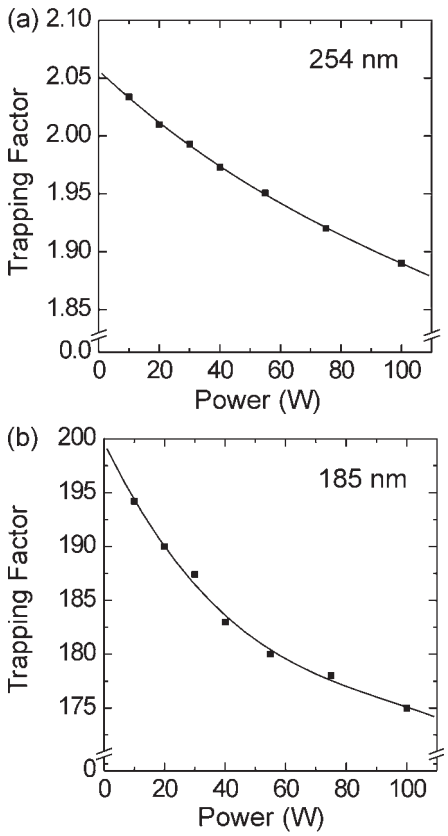

Figure 9. Trapping factor as a function of power for the (*a*) 254 nm and (*b*) 185 nm transitions, keeping the other parameters at the base values. Increasing power increases the importance of electron collision quenching and cataphoresis in redistributing absorbers.

the Hg ground state density, there is more efficient momentum transfer of Hg^+ with the more numerous and same mass ground state Hg compared to the lighter Ar. The rate of symmetric charge exchange also increases, resulting in charge exchange becoming the dominant momentum transfer process which shifts the peak of the Hg ion density towards the walls, as shown in figure 8. This relative shift in ionization peak is more apparent in the Everlight lamp due to the larger distance between the centre of the column and the walls. Due to the shift in peak in ionization, the cataphoresis now occurs at a different location in the lamp.

The peak densities of Hg($6\,^3P_1$) are shifted towards the walls at higher Hg densities in both lamps. The end result is that in the Everlight lamp geometry, regardless of where the photons are emitted in the bulk, they experience a Hg absorber density of around 6×10^{14} cm^{-3} between the sites of emission and the walls. In contrast, most of the photons emitted in the interior of the QL lamp traverse a depleted region of Hg in the centre of the lamp, and only traverse high densities of absorbers near the walls of the lamp. As a result, trapping factors for the Everlight lamp are moderately higher than those for the QL lamp.

Trapping factors as a function of power for the QL lamp are shown in figure 9 for an Ar fill pressure of 500 mTorr and Hg pressure of 5 mTorr. We found that the trapping factors generally decrease with increasing power deposition. With increasing power the depletion of Hg($6\,^1S_0$) in the centre of the lamp by both thermal and cataphoretic processes increases, producing larger ground state densities near the walls. As a result the excited state densities are produced successively closer to the walls with increasing power. Had this been a plane parallel geometry, the proximity of the radiators to the walls would probably have been offset by the larger column density of Hg($6\,^1S_0$) near the walls resulting in little, if any change in trapping factor. In these more complex geometries, the closer proximity of radiators to the walls dominates the increased column density, producing a smaller trapping factor. Increased power also produces more electron collisional quenching. Quanta which were originally emitted deep in the interior of the lamp are less likely to escape the plasma. It is these photons which most heavily contribute to the trapping factor, and so their loss reduces the average residence time and decreases the trapping factor.

To decouple cataphoresis and electron collisional quenching from other parametric variations, investigations were performed at low ICP powers. For example, trapping factors as a function of Ar fill pressure are shown in figure 10 for a power of 10 W, for which cataphoresis is not very important. As such, the densities of excited states of Hg peak in the centre of the lamp, and most quantum are emitted from that volume. The trapping factors are found to be approximately constant over the pressure range studied (50–1500 mTorr) and within the statistical error of the method, a consequence of natural and Doppler broadening dominating. From these and other studies, we concluded that variations of trapping factors with power and pressure over the design space can be largely attributed

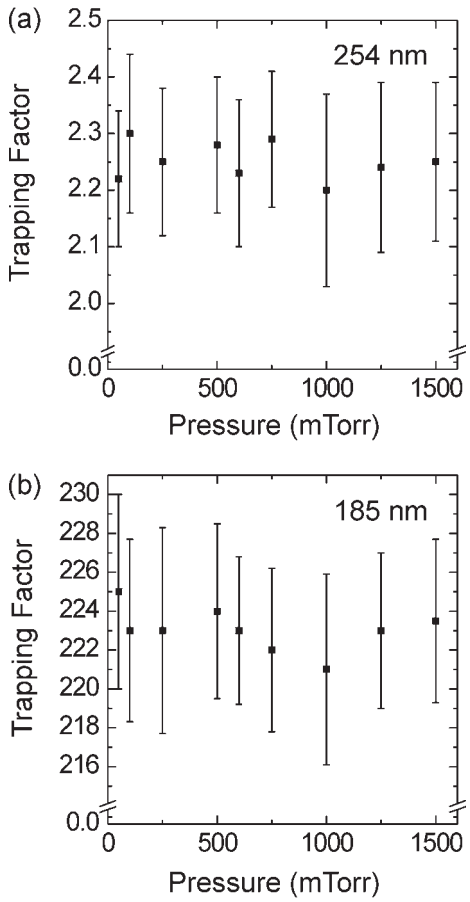

Figure 10. Trapping factor as a function of Ar fill pressure for 10 W for the (*a*) 254 nm and (*b*) 185 nm transitions, keeping the other parameters at the base values.

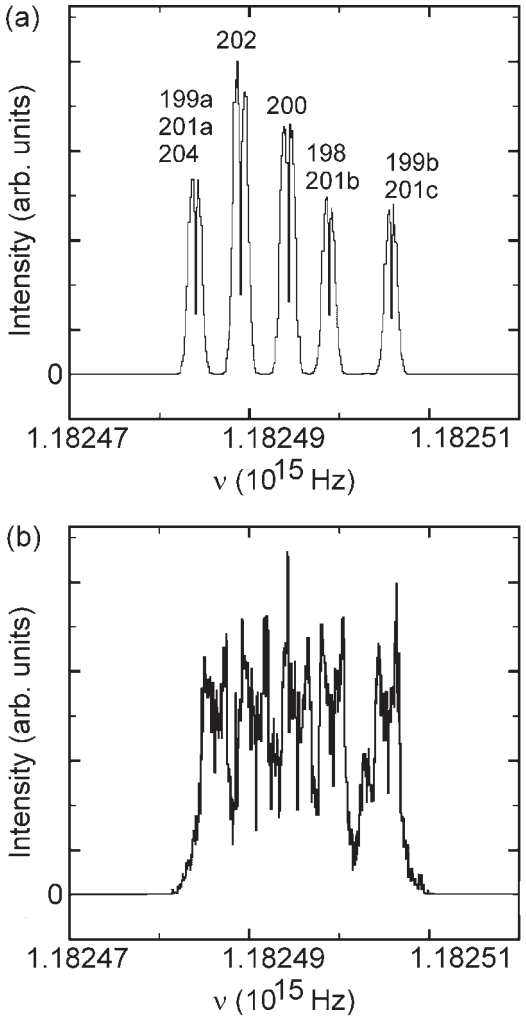

Figure 11. Exit spectra when including the complete isotopic structure of Hg for 55 W. (*a*) 500 mTorr Ar fill pressure, cold spot temperature of 310 K and (*b*) 1.5 Torr Ar fill pressure, cold spot of 340 K. At the lower pressure and temperature, there is little collisional mixing between the isotopes.

to redistribution of radiators resulting from cataphoresis and secondarily due to electron quenching in the bulk of the plasma.

Previous studies have proposed that trapping factors can be manipulated by changing the isotopic abundance of the Hg atoms [35]. The ability to manipulate trapping factors with the addition of, e.g. Hg-196 results from its central frequency being sufficiently far away from the other isotopes that a photon that is emitted by that isotope has a high likelihood of escaping from the lamp. Ideally, quanta of energy which are collisionally mixed between the isotopes and which are preferentially channelled to the Hg-196 isotope are rapidly radiated away. Some success in manipulating radiation trapping factors with isotopic abundances has been achieved for conventional high pressure linear lamps [35].

In this regard, exit spectra for the complete isotopic structure of Hg with hfs are shown in figure 11 for an Ar fill pressure of 500 mTorr, $T_c = 310$ K (Hg = 5 mTorr) and an Ar fill pressure 1.5 Torr, $T_c = 340$ K (Hg = 40 mTorr). Other operating parameters were kept at their base case values. The spectrum at the lower fill pressure and cold spot shows ten peaks due to self-trapping. The Hg-196 isotope is not visible in the spectrum for these conditions due to its low abundance. The isotopes of the Hg-199a, Hg-201a, and Hg-204 have small line centre separations compared to their separations from other isotopes. As a result, their combined lineshape appears as the lineshape for a single isotope. The Hg-198 and Hg-201b isotopes, and the Hg-199b and Hg-201c isotopes also behave similarly. The end result is the appearance of five 'isotopes'. At low Ar and Hg pressures typical of electrodeless lamps, there is insufficient broadening and collisional mixing for there to be a significant exchange of quanta between isotopes and so we obtain non-overlapping spectra with line self-reversal. As such, special isotopic mixtures to manipulate trapping factors are not likely to be important at lower pressures of electrodeless lamps. At the higher Ar and Hg densities typical of conventional linear lamps which have greater collisional broadening and mixing, the lineshapes overlap and there is exchange of quanta between isotopes, as shown in figure 11(*b*). We studied the effect of artificially increasing the Hg-196 concentration on the trapping factors. We found that for Hg-196 concentrations varying from 0.15% (naturally occurring) to 3.5%, there was no significant variation in the trapping factors of any of the Hg isotopes. This is again due to our low pressure operating conditions, for which there are not enough collisional processes to randomize the exit channels of photons.

4. Concluding remarks

A Monte Carlo resonance radiation transport model has been described which interfaces with a plasma equipment model to evaluate radiation trapping in gas discharges having complex geometries. Electrodeless inductively coupled discharges were investigated under a variety of operating conditions with different isotopic considerations. The scaling laws which provide Holstein factors in simpler geometries are not necessarily applicable in the case where radial cataphoresis generates a non-uniform density profile of absorbers and emitters. At typical operating conditions, the electromagnetic skin depth is much larger than the size of the lamp and so the frequency of rf excitation does not affect radiation transport. Trapping factors decrease with an increase in applied power due in large part to a redistribution of radiators and absorbers. The shape of the plasma vessels affects the radiation transport through cataphoresis. This effect increases at higher temperatures where momentum transfer between Hg ions and Hg neutrals is more efficient.

The methodology for obtaining radiation trapping factors just described is computing intensive and requires resources far exceeding those for more convenient analytic or semi-analytic formations. The added computational burden of the radiation transport calculation is, however, only a moderate fraction of the total time required for the plasma hydrodynamics calculation using our model. A legitimate issue is whether the additional resources are justified. For geometries, and spatial distributions of radiators and absorbers which are readily captured in Green's functions, analytic or semi-analytic expressions for trapping factors are clearly the preferred technique. As the complexity of the geometry increases or the ability to analytically predict the distribution of radiators and absorbers diminishes (due to, e.g. the consequences of cataphoresis), the increased complexity of our approach becomes justified for improvements by factors of 2–4 in calculating radiation factors.

Acknowledgments

This work was supported by Osram Sylvania Inc. and the National Science Foundation (CTS99-74962, CTS032-15353). The authors thank Dr G Lister for his insightful advice during the course of this work.

References

[1] Shinomaya M, Kobayashi K, Higashikawa M, Ukegawa S, Matsuura J and Tanigawa K 1991 *J. Ill. Eng. Soc.* **44**
[2] Anderson J M 1970 *US Patent* 3,500,118
[3] Molisch A F and Oehry B P 1998 *Radiation Trapping in Atomic Vapours* (Oxford: Clarendon)
[4] Milne E A 1926 *J. Lond. Math. Soc.* **1** 40
[5] Holstein T 1947 *Phys. Rev.* **72** 1212
[6] Biberman L M 1947 *Zh. Eksp. Theor. Fiz.* **17** 416
[7] van Trigt C 1971 *Phys. Rev.* A **4** 1303
[8] van Trigt C 1976 *Phys. Rev.* A **13** 726
[9] Anderson J B, Maya J, Grossman M W, Lagushenko R and Waymouth J F 1985 *Phys. Rev.* A **31** 2968
[10] Sommerer T J 1993 *J. Appl. Phys.* **74** 1579
[11] Lawler J E, Parker G J and Hitchon W N G 1993 *J. Quant. Spectrosc. Radiat. Transfer* **49** 627
[12] Curry J J, Lawler J E and Lister G G 1999 *J. Appl. Phys.* **86** 731
[13] Lawler J E and Curry J J 1998 *J. Phys. D: Appl. Phys.* **31** 3235
[14] Menningen K L and Lawler J E 2000 *J. Appl. Phys.* **88** 3190
[15] Lawler J E, Curry J J and Lister G G 2000 *J. Phys. D: Appl. Phys.* **33** 252
[16] Lee H J and Verboncoeur J P 2001 *Phys. Plasmas* **8** 3077
[17] Lee H J and Verboncoeur J P 2001 *Phys. Plasmas* **8** 3089
[18] Rauf S and Kushner M J 1997 *J. Appl. Phys.* **81** 5966
[19] Avery L W, House L L and Skumanich A 1969 **9** 519
[20] Lister G G private communication
[21] Jefferies J T and White O 1960 *Astrophys. J.* **132** 767
[22] Rockwood S D 1973 *Phys. Rev.* A **8** 2348
[23] Kenty C 1950 *J. Appl. Phys.* **21** 1309
[24] Vriens L and Smeets A H M 1980 *Phys. Rev.* A **22** 940
[25] Hayashi M 1991 Nagoya Institute of Technology *Report* No IPPJ-AM-19
[26] Tachibana K 1986 *Phys. Rev.* A **34** 1007
[27] Rapp D and Englander-Golden P 1965 *J. Chem. Phys.* **43** 1464
[28] MacFarland R H and Kinney J D 1965 *Phys. Rev.* **137** A1058
[29] Wren D J and Setser D W 1981 *J. Chem. Phys.* **74** 2331
[30] Majetich S, Boczar E M and Wiesenfeld J R 1989 *J. Appl. Phys.* **66** 475
[31] Johnsen R, Leu M T and Biondi M A 1973 *Phys. Rev.* A **8** 1808
[32] Jones J D C, Lister D G, Birkinshaw K and Twiddy N D 1980 *J. Phys.* B **13** 799
[33] Benck E C, Lawler J E and Dakin J T 1989 *J. Opt. Soc. Am.* B **6** 11
[34] Netten A and Verheij C M 1994 QL lighting product presentation storybook (Philips Lighting, Eindhoven, Product Literature, 1991; Updated 1994)
[35] Grossman M W, Lagushenko R and Maya J 1986 *Phys. Rev.* A **34** 4094